

Single-atom transport in optical conveyor belts: Enhanced shortcuts-to-adiabaticity approach

Sascha H. Hauck, Gernot Alber, and Vladimir M. Stojanović

Institut für Angewandte Physik, Technical University of Darmstadt, D-64289 Darmstadt, Germany

(Dated: November 18, 2021)

Fast and nearly lossless atomic transport, enabled by moving the confining trap, is a prerequisite for many quantum-technology applications. While theoretical studies of this problem have heretofore focussed almost exclusively on simplified scenarios (one-dimensional systems, purely harmonic confining potentials, etc.), we investigate it here in the experimentally relevant setting of a moving optical lattice (*optical conveyor belt*). We model single-atom transport in this system by taking fully into account its three-dimensional, anharmonic confining potential. We do so using the established method of shortcuts to adiabaticity (STA), i.e. an inverse-engineering approach based on Lewis-Riesenfeld invariants, as well as its recently proposed modification known as *enhanced* STA (eSTA). By combining well-controlled, advanced analytical techniques and the numerical propagation of a time-dependent Schrödinger equation using the Fourier split operator method, we evaluate atom-transport fidelities within both approaches. Being obtained for realistic choices of system parameters, our results are relevant for future experiments with optical conveyor belts. Moreover, they reveal that in the system at hand the eSTA method outperforms its STA counterpart for all but the lowest optical-lattice depths.

I. INTRODUCTION

Efficient transport of cold neutral atoms [1–11] – either in the form of condensates or individually – is of utmost importance for a variety of emerging quantum-technology applications [12, 13] as well as for quantum-state engineering [14–16]. Such transport, often referred to as “shuttling” [17] and expected to be fast and nearly lossless, entails moving the confining magnetic- [18–20] or optical trap [21, 22]. In particular, moving optical traps come in two varieties – moving optical lattices [9, 11] and tweezers [23–25]. For single-atom transport it is typically required that the final atomic state be as close as possible to the initial one – up to an irrelevant global phase factor – in the rest frame of the moving trap (the high-fidelity condition). This is equivalent to demanding complete absence (or, at least, minimization) of vibrational excitations at the end of transport, but does not rule out the existence of transient excitations at intermediate times [5].

The lack of requirement for adiabaticity throughout atom-transport processes motivates the use of control protocols known as shortcuts to adiabaticity (STA) [26] for their modelling. Generally speaking, the latter lead to the same final states as slow, adiabatic changes of the control parameters of a system, but typically require significantly shorter times to reach that state. This makes the system much less prone to the debilitating effects of noise and decoherence. Importantly, adiabatic processes are those for which slow changes of control parameters leave some dynamical properties of the system invariant. As a consequence, arguably the most useful ones among STA methods are inverse-engineering techniques based on the concept of Lewis-Riesenfeld invariants [27].

While STA protocols have already found applications in a variety of quantum systems [26], their analytical modification – inspired by optimal-control techniques [28]

– has quite recently been proposed and termed *enhanced shortcuts to adiabaticity* (eSTA) [29]. The main motivation behind eSTA is to design efficient control protocols for systems to which STA protocols are not directly applicable. The principal idea of eSTA is to first approximate the full Hamiltonian of such a system by a simpler one for which an STA protocol can be found. Assuming that this STA protocol for the simplified Hamiltonian is close to being optimal even when applied to the full system Hamiltonian, the actual optimal eSTA protocol is obtained through a gradient expansion in the space of control parameters. In principle, the heuristic character of eSTA does not guarantee its superiority over STA and, indeed, the criteria as to when this scheme can be expected to work efficiently are still unknown [29]. Yet, eSTA has already been shown to outperform STA in certain problems of moderate complexity [29], which motivates its use in more complex problems.

Theoretical studies of coherent single-atom transport have heretofore relied on simplified scenarios, typically assuming a one-dimensional geometry (i.e. motion only along the direction of transport) [5, 30] or taking the confining potential to be purely harmonic [2, 6]. However, in realistic systems such idealizations often do not apply, either because there is a significant coupling between the longitudinal and transverse degrees of freedom or because the trapping potential is strongly anharmonic. An important example of such systems is furnished by *optical conveyor belts* (OCBs) [21, 31], moving optical lattices enabled by two counterpropagating Gaussian laser beams with equal intensities, which are slightly mutually detuned. Those systems constitute powerful tools for the precise positioning of atoms [22, 31, 32], with the added capabilities to enable high-speed transport over macroscopic distances and quickly sort atoms into ordered arrays [33–35]. In the context of single-atom transport, OCBs have been investigated quite recently [9, 11].

In this paper, we address single-atom transport in an OCB using both STA and eSTA methods. We model this system by taking fully into account its underlying three-dimensional (3D), anharmonic confining potential. Using an existing inverse-engineering single-atom transport theory [5], we first obtain an STA solution for the trajectory of a moving trap. We then obtain – by combining the obtained STA solution with advanced analytical techniques – an eSTA solution of the same problem. Finally, based on the designed trap trajectories we evaluate the resulting single-atom dynamics through the numerical propagation of a time-dependent Schrödinger equation. We quantify these dynamics by computing atom-transport fidelities for a broad range of lattice depths within both STA and eSTA frameworks.

Given that they correspond to realistic choices of the relevant experimental parameters (beam waists, lattice depths, transport distances, etc.), our obtained results are of utmost interest for future experiments with OCBs. Furthermore, these results show that the eSTA method yields faster single-atom transport than STA for all but the lowest optical-lattice depths.

The remainder of this paper is organized as follows. In Sec. II we introduce the system under consideration and its characteristic length-, time-, and energy scales. Section III discusses the design of trajectories of the moving trap. This is first done using the STA method, i.e. a Lewis-Riesenfeld invariant (Sec. III A), and then using the eSTA method based on the STA solution for a harmonically-approximated OCB potential (Sec. III B). In Sec. IV we briefly describe our methodology for computing the resulting single-atom dynamics. We first review the general aspects of the Fourier split operator method (Sec. IV A), followed by specific details of our implementation thereof (Sec. IV B). Our findings are presented and discussed in Sec. V, starting with the atom-transport fidelities obtained for a broad range of system parameters using the STA and eSTA methods (Sec. V A), and followed by a comparison of the latter results with alternative approaches (Sec. V B). We conclude, with a short summary of the paper and some general remarks, in Sec. VI. Some involved mathematical derivations are relegated to Appendices A and B, while Appendix C summarizes certain intermediate calculation results.

II. SYSTEM AND ITS HAMILTONIAN

We consider an atom of mass m in an OCB, whose optical axis is in the z direction. In what follows, we will be concerned with the problem of transporting an atom to a distant location – the distance being at least an order of magnitude larger than the size of the atomic wave packet – along this same (longitudinal) direction. This mimics the physical situation encountered in typical experimental setups [9, 11]. The initial- and target atomic states are assumed to be the ground states of the OCB potential centered at two different locations.

The relevant single-atom Hamiltonian reads

$$H_{\text{OCB}} = -\frac{\hbar^2 \nabla^2}{2m} + U_{\text{F}}(x, y, z), \quad (1)$$

where $U_{\text{F}}(x, y, z)$ is the full 3D potential of an OCB: [9]

$$U_{\text{F}}(x, y, z) = U_{f,0}(z) \cos^2(kz) \times \exp\left(-2\left[\frac{x^2}{w_x(z)^2} + \frac{y^2}{w_y(z)^2}\right]\right). \quad (2)$$

Here $k = 2\pi/\lambda$ is the wave number of the dipole-trap laser with wavelength λ . The lattice depth $U_{f,0}(z)$ is given by

$$U_{f,0}(z) = C \frac{P_0}{w_x(z)w_y(z)}, \quad (3)$$

where $w_x(z)$, $w_y(z)$ are the two transverse beam waists, which depend on the longitudinal position z :

$$w_{x/y}(z) = w_{x/y,0} \sqrt{1 + \left(\frac{z}{Z_{R,x/y}}\right)^2}, \quad (4)$$

with $Z_{R,x}$ and $Z_{R,y}$ being the respective Rayleigh lengths. In Eq. (3) P_0 stands for the output laser power, while the constant $C = \hbar\Gamma^2/(2\Delta I_0)$ characterizes the concrete experimental setup, with the saturation intensity I_0 , the decay rate Γ , and the detuning $\Delta = \omega - \omega_0$ between the laser frequency ω and the frequency ω_0 of the relevant atomic transition (e.g. $\omega_0 = 2\pi \times 384.23$ THz for the Rubidium D_2 -line [36]).

Finding a harmonic approximation $V(x, y, z)$ of the full OCB potential U_{F} in Eq. (2) is of crucial interest for our further considerations. This simplified potential can readily be found by applying a harmonic approximation to various terms in U_{F} . To this end, we first assume $z/Z_{R,x} \ll 1$ and $z/Z_{R,y} \ll 1$. We also assume that $x/w_{x,0} \ll 1$, $y/w_{y,0} \ll 1$, and that $kz \ll 1$. Under these assumptions, it is straightforward to find that

$$V(x, y, z) = -U_0 + \frac{m}{2} (\omega_x^2 x^2 + \omega_y^2 y^2 + \omega_z^2 z^2), \quad (5)$$

where $U_0 \equiv U_{f,0}(0)$ is the potential depth at the focus of the beam and the frequencies ω_x , ω_y , and ω_z are respectively given by

$$\begin{aligned} \omega_x^2 &= \frac{4U_0}{mw_{x,0}^2}, \\ \omega_y^2 &= \frac{4U_0}{mw_{y,0}^2}, \\ \omega_z^2 &= \frac{U_0}{m} \left(Z_{R,x}^{-2} + Z_{R,y}^{-2} + 2k^2 \right). \end{aligned} \quad (6)$$

It is useful to note that in the paraxial approximation $Z_{R,x/y} \gg 1/k$, which is always valid for OCBs, one has that $\omega_z^2 \approx 2U_0 k^2/m$. By taking into account Eqs. (6) and the well-known relation $Z_{R,x/y} = kw_{x/y,0}^2/2$, one concludes that there are five independent parameters in the

system at hand: the transport distance d , the final time t_f , the waists $w_{x/y,0}$, and the potential depth U_0 .

To facilitate our further discussion, it is prudent to single out the characteristic time-, length-, and energy scales in the system under consideration. The time $\tau_z = 2\pi/\omega_z$ corresponding to the harmonic-oscillator frequency ω_z in the z direction [cf. Eq. (5)] will be used in what follows as the characteristic timescale. On the other hand, the harmonic-oscillator length $l_z \equiv \sqrt{\hbar/(2m\omega_z)}$ in the z direction will serve as the characteristic lengthscale. Finally, all energies in the problem will be expressed in units of the recoil energy $E_R \equiv \hbar^2 k^2/(2m)$.

III. STA AND eSTA TRAP TRAJECTORIES

Among all STA methods [26], invariant-based inverse engineering established itself as the method of choice in the context of efficient atom transport. The basic invariant-based inverse engineering transport theory was developed in Ref. [5]. The crux of that theory is the use of quadratic-in-momentum invariants relevant for transport problems, which were first discussed by Lewis and Riesenfeld [27]. Importantly, it was also demonstrated in Ref. [5] that the case of a harmonic trapping potentials and that of an arbitrary potential require different treatments, as the perfect atom transport in the latter case necessitates – in principle – compensating forces in the reference frame moving with the trap (cf. Sec. IV B below).

In the following, we first apply the theory developed in Ref. [5] to our problem of single-atom transport in OCBs. To be more precise, we determine the classical path of the potential minima in a moving trap in the problem at hand (Sec. III A). We then apply the eSTA scheme, based on the theory recently laid out in Ref. [29], to address the same problem (Sec. III B). We do so by making use of a single-atom Hamiltonian with the harmonically approximated OCB potential $V(x, y, z)$ [cf. Eq. (5)] as the simplified Hamiltonian of the system for which an STA-based protocol can readily be obtained.

A. Trajectory of the moving trap: STA solution

A dynamical invariant of a time-dependent Hamiltonian $H(t)$ is an operator $I(t)$, which satisfies the equation

$$\frac{\partial}{\partial t} I(t) + [H(t), I(t)] = 0. \quad (7)$$

The eigenvalues λ_n of the invariant $I(t)$ are constant in time. Assuming that these eigenvalues are non-degenerate, the corresponding eigenstates $|\Phi_n(t)\rangle$ and the instantaneous eigenstates $|\Psi_n(t)\rangle$ of the Hamiltonian $H(t)$ (the so-called transport modes) satisfy the simple relation $|\Psi_n(t)\rangle = e^{i\theta_{\text{LR}}(t)} |\Phi_n(t)\rangle$, where $\theta_{\text{LR}}(t) = \hbar^{-1} \int_0^t \langle \Phi_n(t') | [i\hbar \partial_{t'} - H(t')] | \Phi_n(t') \rangle dt'$ is the

Lewis-Riesenfeld phase [26]. The general solution of the Schrödinger equation for the Hamiltonian $H(t)$ can then be written in the form

$$|\Psi(t)\rangle = \sum_n C_n e^{i\theta_{\text{LR}}(t)} |\Phi_n(t)\rangle. \quad (8)$$

It is worth noting that for very long evolution times ($t \rightarrow \infty$) Eq. (7) results in the adiabatic-following condition $[H(t), I(t)] \approx 0$.

In what follows, we apply Lewis-Riesenfeld theory to the approximate OCB Hamiltonian

$$H_0 = -\frac{\hbar^2 \nabla^2}{2m} + V(x, y, z - q_0(t)), \quad (9)$$

i.e. a single-atom Hamiltonian with the simplified harmonic potential $V(x, y, z)$ of Eq. (5). For our transport scheme we make use of the time-dependent, quadratic-in-momentum invariant [5]

$$I = \frac{1}{2m} (p - m\dot{q}_{c,z})^2 + \frac{m}{2} \omega_z^2 (z - q_{c,z})^2, \quad (10)$$

where $q_{c,z}$ is the z component of the classical path for the trapped particle. Importantly, there are auxiliary equations that must be fulfilled in order to use this invariant [5]. For simple displacement schemes the auxiliary equation has the form characteristic of a forced harmonic oscillator. It reads

$$\ddot{q}_{c,z}(t) + \omega_z^2 [q_{c,z}(t) - q_0(t)] = 0, \quad (11)$$

where $q_0(t)$ is the trajectory of the potential minimum.

In order to fulfill the appropriate boundary conditions for the “classical” particle, we are choosing a polynomial Ansatz of ninth degree, by which the general solution for the path of the potential minima can be obtained through Eq. (11). This results in

$$q_0(t) = d \sum_{n=3}^9 b_n \left(\frac{t}{t_f}\right)^n \quad (12)$$

with the following solution vector for constants b_n :

$$\mathbf{X}_{q_0} = \begin{pmatrix} b_3 \\ b_4 \\ b_5 \\ b_6 \\ b_7 \\ b_8 \\ b_9 \end{pmatrix} = \begin{pmatrix} 2520(t_f\omega_z)^{-2} \\ -12600(t_f\omega_z)^{-2} \\ 22680(t_f\omega_z)^{-2} + 126 \\ -17640(t_f\omega_z)^{-2} - 420 \\ 5040(t_f\omega_z)^{-2} + 540 \\ -315 \\ 70 \end{pmatrix}. \quad (13)$$

The obtained classical path of the potential minimum for different final times t_f is shown in Fig. 1.

B. Trajectory of the moving trap: eSTA solution

Generally speaking, the first step in applying the eSTA method to a system with the Hamiltonian H_S entails obtaining an STA solution for a “close” Hamiltonian H_0 [29]; this solution is parameterized by a vector

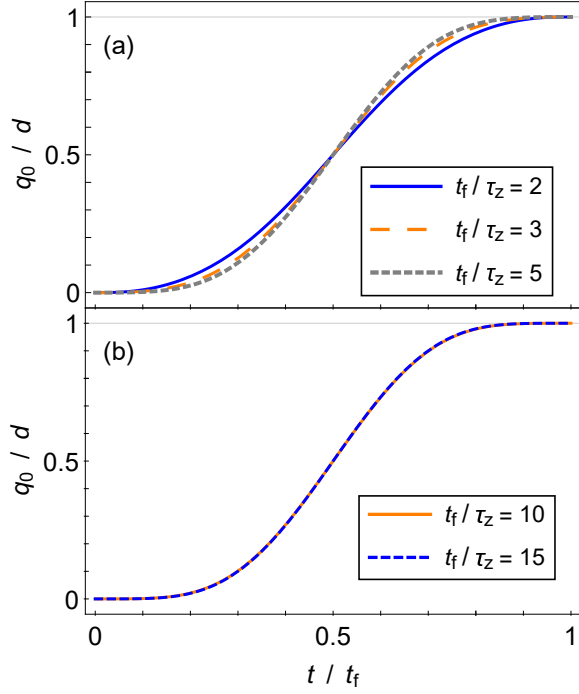


FIG. 1: (Color online) Path of the potential minimum as a function of time, obtained using the STA approach, for transport times t_f (a) comparable to, and (b) an order of magnitude longer than the internal timescale τ_z .

$\lambda_0 \in \mathbb{R}^n$. In the present context, the meaning of “close” is that there exists a parameter μ_S such that H_S can be expressed in the form of a series expansion

$$H_S = \sum_{k=0}^{\infty} \mu_S^k H^{(k)}, \quad (14)$$

such that $H^{(0)} \equiv H_0$. In the OCB system at hand, the role of H_S is played by the Hamiltonian H_{OCB} of Eq. (1), in which z is replaced by $z - q_0(t)$. On the other hand, the role of H_0 is played by the Hamiltonian of Eq. (9).

Because we aim to find an optimal solution for the full Hamiltonian H_S based on an available STA solution for H_0 , it is prudent to express the general control vector for the full system in the form $\lambda = \lambda_0 + \alpha$, i.e. as a sum of the STA control vector λ_0 and an auxiliary control vector α . The value of α that corresponds to the optimal solution, i.e. the correction vector necessary to obtain the optimal eSTA protocol will be denoted by ϵ in the following.

A crucial assumption within the eSTA scheme is that the protocol based on the existing STA solution for H_0 is close to being optimal even when applied to the full system Hamiltonian H_S [29]. Furthermore, one assumes that the fidelity is quadratic around its maximal value, resulting in the approximate relation [29]

$$F\left(\mu_S, \lambda_0 + \alpha \frac{\nabla F(\mu_S, \lambda_0)}{\|\nabla F(\mu_S, \lambda_0)\|}\right) \approx 1 - c(\alpha - \epsilon)^2, \quad (15)$$

where $\epsilon \equiv \|\epsilon\|$, $\alpha \equiv \|\alpha\|$, and c is a positive constant. Us-

ing the above assumptions and a Taylor expansion of the left-hand-side of Eq. (15) around $\alpha = \epsilon$, it is straightforward to find that [29]

$$\epsilon \approx \frac{2[1 - F(\mu_S, \lambda_S)] \nabla F(\mu_S, \lambda_0)}{\|\nabla F(\mu_S, \lambda_0)\|^2}. \quad (16)$$

As derived in Ref. [29], the fidelity can be approximated up to second order in μ_S as

$$F(\mu_S, \lambda_S) \approx 1 - \frac{1}{\hbar^2} \sum_{n=1}^{\infty} |G_n|^2, \quad (17)$$

with G_n being an auxiliary (scalar) function, given by

$$G_n = \int_0^{t_f} dt \langle \Psi_n(t) | [H_S(\lambda_0; t) - H_0(\lambda_0; t)] | \Psi_0(t) \rangle, \quad (18)$$

and $|\Psi_n(t)\rangle$ the transport modes of the idealized Hamiltonian H_0 [cf. Sec. III A]. An analogous approximate expression, up to second order in μ_S , for the gradient of the fidelity reads [29]

$$\nabla F(\mu_S, \lambda_0) \approx -\frac{2}{\hbar^2} \sum_{n=1}^{\infty} \text{Re}(G_n \mathbf{K}_n^*), \quad (19)$$

where \mathbf{K}_n is another auxiliary (vector) function:

$$\mathbf{K}_n = \int_0^{t_f} dt \langle \Psi_n(t) | \nabla_{\lambda} H_S(\lambda; t) |_{\lambda=\lambda_0} | \Psi_0(t) \rangle. \quad (20)$$

The optimal correction vector ϵ can be recast in terms of the auxiliary functions G_n and \mathbf{K}_n as

$$\epsilon = -\frac{\left(\sum_{n=1}^N |G_n|^2\right) \sum_{n=1}^N \text{Re}(G_n^* \mathbf{K}_n)}{\left\|\sum_{n=1}^N \text{Re}(G_n^* \mathbf{K}_n)\right\|^2}, \quad (21)$$

where N is the cut-off parameter. This vector can be computed numerically once the expressions for G_n and \mathbf{K}_n are obtained by evaluating the integrals in Eqs. (18) and (20), respectively. In the atom-transport problem at hand, where the states $|\Psi_n(t)\rangle$ represent the transport modes of the 3D harmonic-oscillator Hamiltonian in Eq. (9), this entails highly nontrivial derivations based on various properties of Hermite polynomials (for details, see Appendices A and B).

For displacement schemes the control vector λ has to fulfill the conditions $q_0(\lambda; jt_f/7) = \lambda_j$ for $j = 1, \dots, 6$. Now the optimized path can be expressed through the path of the simplified problem

$$q_0(\lambda; t) = q_0(\lambda_0; t) + f(\alpha; t), \quad (22)$$

with $q(\lambda; jt_f/7) = \lambda_{0,j} + \alpha_j$ for $j = 1, \dots, 6$. The auxiliary function $f(\alpha; t)$ has to obey the following boundary conditions:

$$\begin{aligned} f(\alpha; 0) &= f(\alpha; t_f) = 0, \\ f(\alpha; jt_f/7) &= \alpha_j \quad (j = 1, \dots, 6), \\ \frac{d^{(n)}}{dt^{(n)}} f(\alpha; t') &|_{t'=\{0, t_f\}} = 0 \quad (n = 1, \dots, 4). \end{aligned} \quad (23)$$

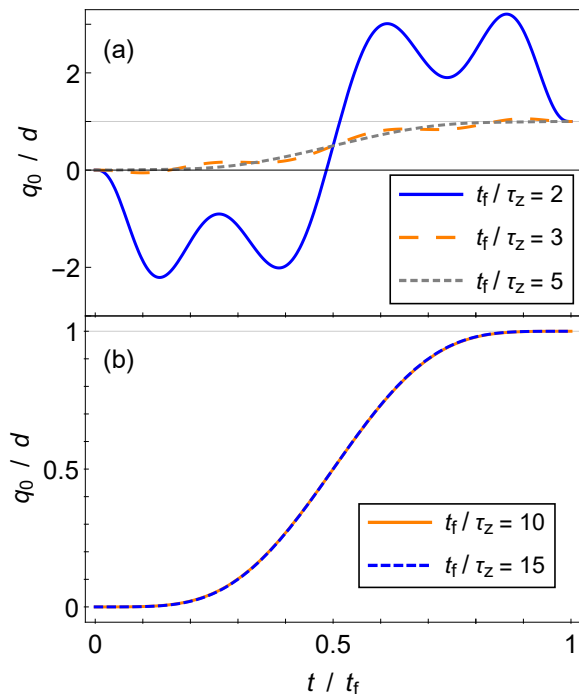


FIG. 2: (Color online) Path of the potential minimum as a function of time, obtained using the eSTA approach, for transport times t_f (a) comparable to, and (b) an order of magnitude longer than the internal timescale τ_z . The parameters chosen are the following: $U_0 = 60 E_R$, $d = 85 l_z$, and $w_{0,x} = w_{0,y} = 4.2 \times 10^6 l_z$.

The latter conditions are chosen such that $f(\boldsymbol{\alpha}; t)$ can be controlled through $\boldsymbol{\alpha}$ and also obeys the conditions of continuity. Therefore, we choose the following polynomial Ansatz of eleventh degree:

$$f(\boldsymbol{\alpha}; t) = \sum_{n=0}^{11} \sum_{k=1}^6 \tilde{a}_{n,k} \alpha_k \left(\frac{t}{t_f} \right)^n. \quad (24)$$

The specific values for the coefficients $\tilde{a}_{n,k}$ in the last equation are given in Table I in Appendix C.

For the optimal eSTA solution, we set the auxiliary control vector $\boldsymbol{\alpha}$ equal to the optimal correction vector $\boldsymbol{\epsilon}$. The latter can be calculated using the general expression in Eq. (21). Because in our 3D problem the transport modes can be enumerated using three 1D quantum numbers $\{n_x, n_y, n_z\}$, we can rewrite the sum in Eq. (21) in terms of the main quantum number n and $\{n_x, n_y, n_z\}$. For the cut-off parameter we take the value $N = 2$, even though our numerical evaluation shows that already taking $N = 1$ yields essentially the same result.

The classical path of the potential minimum, obtained using the eSTA approach, is depicted in Fig. 2. What can be inferred by comparing this path to the one obtained using the STA approach (Fig. 1) is that their shapes differ significantly only for short transport times.

IV. SINGLE-ATOM DYNAMICS: THE FOURIER SPLIT OPERATOR METHOD

Having described the design of trap trajectories within both STA and eSTA schemes in Sec. III, in the following we briefly present our chosen approach for evaluating the resulting single-atom dynamics using the Fourier split operator method (FSOM). We start with a brief reminder of the basics of the FSOM (Sec. IV A), followed by the specific details of our own implementation thereof to the single-atom transport problem (Sec. IV B).

A. Basics of the FSOM

The FSOM is customarily used for solving Cauchy-type initial-value problems of the type

$$\frac{\partial}{\partial t} f(\mathbf{x}, t) = \hat{A}(t) f(\mathbf{x}, t), \quad (25)$$

with some (possibly time-dependent) operator $\hat{A}(t)$ and the initial condition $f(\mathbf{x}, t) = f_0(\mathbf{x})$. The method is typically used in cases where the operator $\hat{A}(t)$ can be written as a sum $\hat{A}(t) = \hat{A}_1(t) + \hat{A}_2(t)$ of two operators, such that $\hat{A}_1(t)$ can easily be diagonalized in real space, while $\hat{A}_2(t)$ is straightforward to diagonalize in Fourier space. In particular, the time-dependent Schrödinger equation (hereafter abbreviated as TDSE) fulfills this requirement, hence the use of the FSOM for solving this type of equations [37, 38]. This requirement allows one to approximate the time-evolution operator of the system by a product of operators that are diagonal either in real- or in Fourier space, the central idea of the FSOM.

In the problem at hand, we make use of the FSOM to determine the final atomic state after displacement by a certain distance. The relevant TDSE corresponds to the Hamiltonian of the type $H(\mathbf{r}, t) = -\hbar^2 \nabla^2 / (2m) + W(\mathbf{r}, t)$, where the potential W pertains to a moving trap and is, consequently, time-dependent (for details, see Sec. IV B below). As a result, the exact time-evolution operator of the system is given by the most general expression that involves a time-ordered product.

By expanding the time-evolution operator $U(t + \delta t, t)$ of the system to third order in δt , we obtain:

$$U(t + \delta t, t) = \exp \left[-\frac{i}{\hbar} \int_t^{t+\delta t} H(\mathbf{r}, t) dt \right] + O[(\delta t)^3]. \quad (26)$$

By making use of the Baker-Campbell-Hausdorff formula [39], the last equation gives an explicit second-order accurate time-stepping scheme for the propagation of the wave-function $\Psi(\mathbf{r}, t)$ [40]:

$$\begin{aligned} \Psi(\mathbf{r}, t + \delta t) &= \exp \left[-\frac{i}{\hbar} W(\mathbf{r}, t) \frac{\delta t}{2} \right] \exp \left(i \frac{\hbar \nabla^2}{2m} \delta t \right) \\ &\times \exp \left[-\frac{i}{\hbar} W(\mathbf{r}, t) \frac{\delta t}{2} \right] \Psi(\mathbf{r}, t) + O[(\delta t)^3]. \end{aligned} \quad (27)$$

The last equation allows one to treat the different exponential terms independently, resulting in the possibility of Fourier-transforming the kinetic term to momentum space. As a result, the complexity of applying an operator on the wave-function Ψ reduces to that of multiplying Ψ by a complex number. Importantly, one can recast the right-hand-side of Eq. (27) using the identity

$$\begin{aligned} & \exp\left(i\frac{\hbar\nabla^2}{2m}\delta t\right) \exp\left[-\frac{i}{\hbar}W(\mathbf{r},t)\frac{\delta t}{2}\right] \Psi(\mathbf{r},t) = \\ & F^{-1}\left[\exp\left(-i\frac{\hbar k^2}{2m}\delta t\right) F\left[\exp\left[-\frac{i}{\hbar}W(\mathbf{r},t)\frac{\delta t}{2}\right] \Psi(\mathbf{r},t)\right]\right], \end{aligned} \quad (28)$$

where F is the Fourier transform and F^{-1} its inverse.

A general solution at time $t' = t + N_t\delta t$ is obtained numerically by applying the single-step propagation of Eq. (27) consecutively N_t times to our initial wave-function $\Psi(\mathbf{r},t)$. In an actual numerical implementation of the FSOM, this last wave-function is discretized on a rectangular regular lattice of N_s points and the continuous Fourier transform is approximated by a discrete one. The computational complexity of propagating the function $\Psi(\mathbf{r},t)$ is dominated by the transformation into Fourier space and back into real space [cf. Eq. (28)]. If these transformations are carried out using the fast Fourier transform (FFT) algorithm [41], an elementary step in the FSOM requires $O(N_s \log_2 N_s)$ operations.

Apart from using the FSOM for computing single-atom dynamics, we also utilize this method to find the ground state of our OCB trapping potential [37]. Let $\phi(\mathbf{r}) = \sum_{j=0}^N c_j \Psi_j(\mathbf{r})$ be an arbitrary trial state with a nonzero overlap with the sought-after ground state $\Psi_0(\mathbf{r})$. Assuming that $\phi(\mathbf{r})$ is the initial ($t = 0$) state in a dynamical evolution of the system, its counterpart at a later time t is given by

$$\phi(\mathbf{r},t) = \sum_{j=0}^N \exp(-iE_j t/\hbar) c_j \Psi_j(\mathbf{r}). \quad (29)$$

By switching from real to imaginary time, i.e. performing a Wick rotation into the complex plane, this last state can be recast as a sum of exponentially-decaying contributions of different eigenstates $\Psi_j(\mathbf{r})$, with the decay rates given by the corresponding eigenvalues E_j . Because the relative contribution of the excited states decays faster than that of the ground state, these contributions become negligible for long enough evolutions. This enables one to extract the desired ground-state energy E_0 and the corresponding wave function $\Psi_0(\mathbf{r})$.

B. TDSE in the comoving frame

Due to time restrictions and storage capabilities, we are restricting ourselves to the displacement of one single trap minimum. Furthermore, we are switching from the lab frame to the *comoving* frame, i.e. the frame moving

along with the trap. This change is accounted for by applying the unitary displacement operator [42]

$$\mathcal{U} = e^{ip_z q_0(t)/\hbar} e^{-imz\dot{q}_0(t)/\hbar} \quad (30)$$

to transform the relevant lab-frame TDSE:

$$i\hbar \frac{\partial}{\partial t} \Psi(\mathbf{r},t) = \left[-\frac{\hbar^2 \nabla^2}{2m} + U_F(x,y,z - q_0(t)) \right] \Psi(\mathbf{r},t). \quad (31)$$

As a result, the time-evolution for the relevant wave-function $\Phi(\mathbf{r},t) \equiv \mathcal{U}\Psi(\mathbf{r},t)$ in the comoving frame is governed by another TDSE:

$$\begin{aligned} i\hbar \frac{\partial}{\partial t} \Phi(\mathbf{r},t) = & \left[-\frac{\hbar^2 \nabla^2}{2m} + \frac{m}{2} \dot{q}_0(t)^2 \right. \\ & \left. + m\ddot{q}_0(z + q_0) + U_F(\mathbf{r}) \right] \Phi(\mathbf{r},t). \end{aligned} \quad (32)$$

The two terms $m\dot{q}_0(t)^2$ and $m\ddot{q}_0 q_0$ result only in time-dependent global phase factors and can hereafter be safely neglected. One advantage of switching to the comoving frame is that we do not have to compute the initial potential after every time step, but just the correction term $m\ddot{q}_0 q$ linear in the acceleration of the potential minimum. In addition, we can restrict our “simulation window” around the potential minimum, which obviates the need to take the whole expanded space of the transport process into account.

Using the result from Eq. (32), one time step in the FSOM for our system can be written in the form

$$\begin{aligned} \Phi(\mathbf{r},t + \delta t) \approx & \exp\left[-\frac{i}{\hbar}U_F(\mathbf{r})\frac{\delta t}{2}\right] F^{-1}\left[\exp\left(-i\frac{\hbar k^2}{2m}\delta t\right) \right. \\ & \times \exp\left[-i\frac{k_z}{2}\delta\dot{q}_0(t)\delta t\right] F\left(\exp\left[-\frac{i}{\hbar}z\delta\dot{q}_0(t)\delta t\right] \right. \\ & \left. \left. \times \exp\left[-\frac{i}{\hbar}U_F(\mathbf{r})\frac{\delta t}{2}\right] \Phi(\mathbf{r},t)\right)\right] + O[(\delta t)^3], \end{aligned} \quad (33)$$

with the velocity difference $\delta\dot{q}_0(t) \equiv \dot{q}_0(t + \delta t) - \dot{q}_0(t)$. This equation is slightly more elaborate than Eq. (28), because the higher-order contributions resulting from the correction term $m\ddot{q}_0 q$ were already treated. Therefore, the higher-order correction terms result solely from the application of the Baker-Campbell-Hausdorff formula and the neglect of the time-ordered product. These terms depend on the commutators of the type $[U_F(\mathbf{r}), p^2]$, as well as the commutators $[H(t_1), H(t_2)]$ involving the Hamiltonian of the system at different times.

It should be stressed that by introducing a linear force of the form $F(t) = m\ddot{q}_0(t)$ in the lab frame, the resulting TDSE in the comoving frame [cf. Eq. (32)] would not contain the term $m\ddot{q}_0 q_0$. This is the so-called “compensating-force approach” and results in the same TDSE as in the lab frame (up to global phase factors) and the ensuing perfect state transfer. Yet, this method is much more challenging to implement experimentally for neutral atoms [43] and even impossible for systems containing trapped ions of more than one sort [44].

V. RESULTS AND DISCUSSION

A. Atom-transport fidelity: STA vs. eSTA

In what follows, we present and analyze our results for the single-atom dynamics in an OCB, obtained using the FSOM and the trap trajectories resulting from the STA and eSTA schemes [cf. Sec. III]. The main figure of merit quantifying this process is the atom-transport fidelity $\mathcal{F}(t_f) = |\langle \Psi_{\text{target}} | \Psi(t_f) \rangle|^2$, which is determined by the module of the overlap of the target state $|\Psi_{\text{target}}\rangle$ (the ground state of the displaced OCB potential) and the final atomic state $|\Psi(t_f)\rangle$. The dependence of the fidelity on the transport time t_f is illustrated for different optical-lattice depths U_0 in Figs. 3 – 5. These results correspond to the same transport distance $d = 85 l_z$, while the waists in the transverse directions were set to $w_{x/y,0} = 4.2 \times 10^6 l_z$.

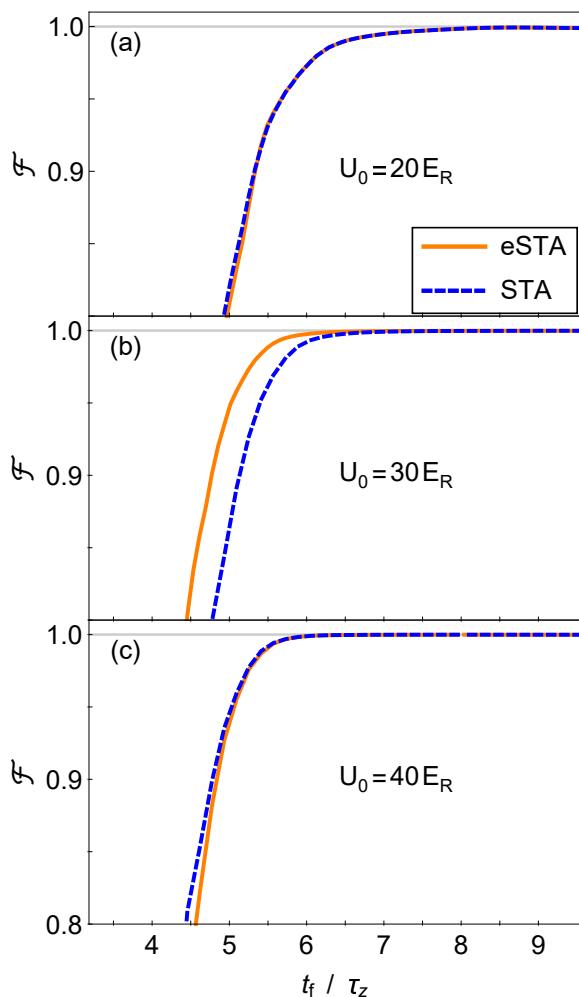


FIG. 3: (Color online) The dependence of the atom-transport fidelity on the transport time t_f , for a potential depth U_0 of (a) $20 E_R$, (b) $30 E_R$, and (c) $40 E_R$. The transport distance d was set to $85 l_z$, while the transverse beam waists are $w_{x/y,0} = 4.2 \times 10^6 l_z$.

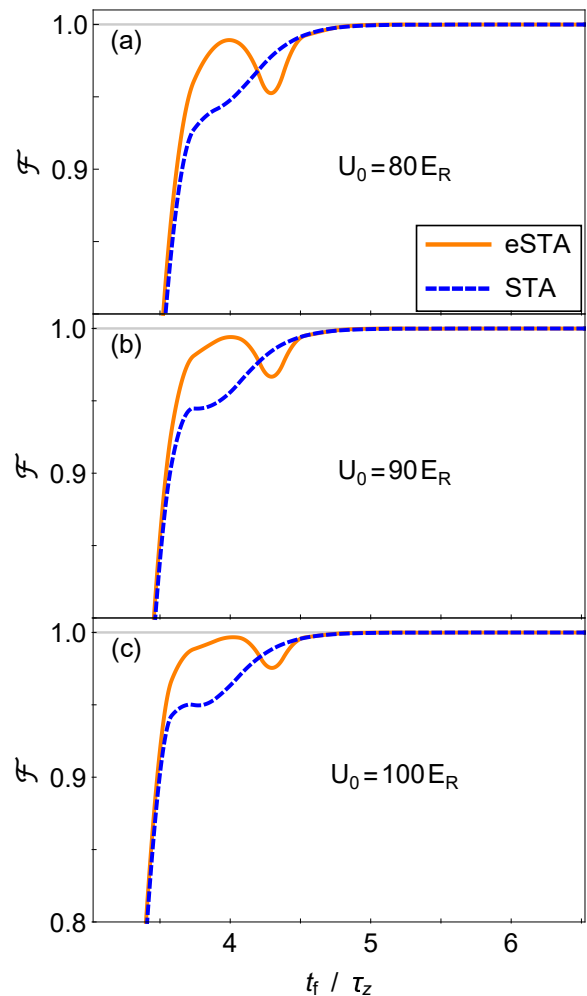


FIG. 4: (Color online) The dependence of the atom-transport fidelity on the transport time t_f , for a potential depth U_0 of (a) $80 E_R$, (b) $90 E_R$, and (c) $100 E_R$. The transport distance d was set to $85 l_z$, while the transverse beam waists are $w_{x/y,0} = 4.2 \times 10^6 l_z$.

One of the salient features of the obtained results is the collapse of the fidelity for short transport times t_f , which is evident from Figs. 3 – 5. This collapse is, generally speaking, a consequence of the fact that the potential itself can only withstand an atomic acceleration below a certain maximal value $|a_{\text{max}}|$ before the atom effectively escapes from the trap and the corresponding fidelity drops rapidly. Namely, in the non-inertial reference frame that moves with the atom the total lattice potential acquires an additional contribution that is linear in the longitudinal coordinate, thus effectively leading to a tilted standing-wave potential in this accelerating frame. As a result, the local minima of the standing wave disappear completely for accelerations above $|a_{\text{max}}| = U_0 k/m$ [31]. Being proportional to U_0 , this maximal acceleration becomes greater for deeper potentials [9].

The collapse of the transport takes place when the

maximal acceleration reached by an atom during the transport process, which will be denoted by $|\tilde{a}_{\max}|$ in the following, exceeds $|a_{\max}|$. While the lower bound on $|\tilde{a}_{\max}|$ is quite generally given by $2d/t_f^2$ [5], its actual value depends on the concrete chosen trap trajectory, i.e. the path of the potential minimum. In particular, for the trajectory obtained using the STA approach in Sec. III A [cf. Eq. (13)], this value is given by $|\tilde{a}_{\max}| \approx 9.372 d/t_f^2$. The fact that for a fixed transport distance $|\tilde{a}_{\max}|$ is inversely proportional to t_f^2 implies that for deeper potentials (i.e. for a higher $|a_{\max}| \propto U_0$) the actual maximal atomic acceleration $|\tilde{a}_{\max}|$ reaches the value of $|a_{\max}|$ at shorter transport times t_f . In other words, for deeper potentials the collapse of the fidelity takes place for shorter times t_f . This is consistent with our numerical findings, illustrated in Figs. 3 – 5 for gradually increasing potential depths. As can be inferred from these results, the characteristic transport times t_f pertaining to the occurrence of the collapse are around 4.5, 3.4, and 2.8 τ_z , respectively, in Figs. 3 – 5 and clearly show the trend of decreasing with the increase of the lattice depth.

Because for eSTA the modulations of the potential path through the optimization vector ϵ are small contributions to the overall dynamics [cf. Sec. III B], for deep-enough lattices the collapse of the fidelity for eSTA-based atom transport takes place at approximately the same transport times as for the corresponding STA scheme. However, it should be stressed that for more shallow lattices (e.g. potential depths U_0 of 30, 50, and 60 E_R) the transport time t_f corresponding to the collapse can be notably different between STA and eSTA. This is due to the fact that even small modulations (such as the modulation through the optimization vector ϵ) can result in non-negligible differences between the maximal atomic accelerations for STA and eSTA. This depends primarily on the modulation strength around the intermediate transport times for which the maximal possible acceleration is exceeded in STA-based transport. On the other hand, this also depends on the sign of the modulation, i.e. whether the modulation leads to higher or lower atomic accelerations $|\tilde{a}_{\max}|$.

Another interesting feature of the results obtained using the eSTA scheme is the slowly forming dip for deeper potentials, as can be observed, e.g., in Fig. 4(a) for $t_f \approx 4.4 \tau_z$. The existence of this dip is a result of increasing transient excitation energies during the transport process upon shortening the transport time t_f . Namely, as first discussed in Ref. [5], the time-averaged transient excitation energy depends on t_f according to $\bar{E}_{p,\min} \propto t_f^{-4}$. Consequently, the implications of the anharmonic character of potential become more and more prominent, i.e. the assumption of the harmonic potential for the STA method begins to break down, resulting in a worse performance of this method. At the same time, the performance of the eSTA approach becomes better for deeper potentials and slowly approaches a perfect transport up until the aforementioned collapse of the transport process. This performance improvement

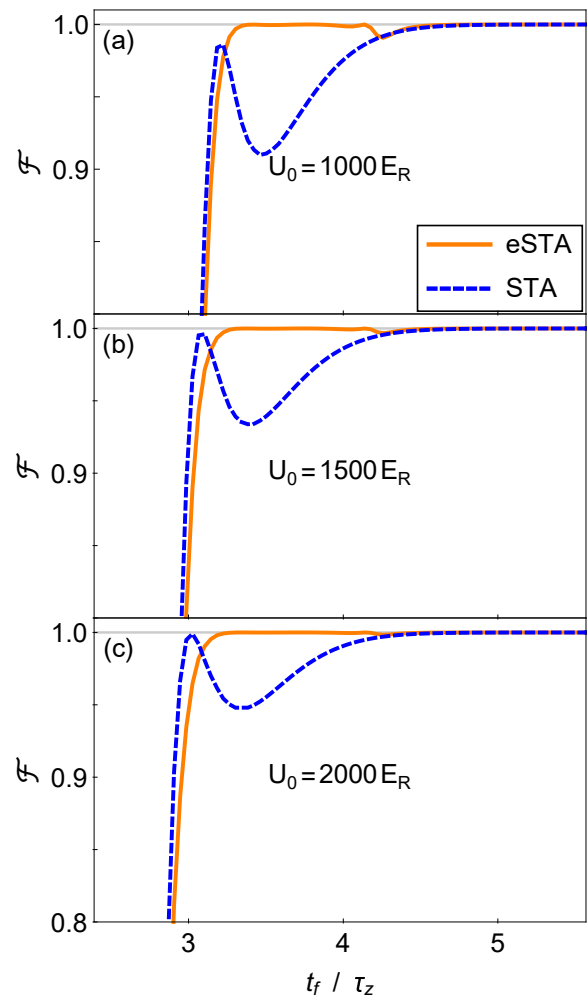


FIG. 5: (Color online) The dependence of the atom-transport fidelity on the transport time t_f , for a lattice depth U_0 of (a) 1000 E_R , (b) 1500 E_R , and (c) 2000 E_R . The transport distance d was set to $85 l_z$, while the transverse beam waists are $w_{x/y,0} = 4.2 \times 10^6 l_z$.

of the eSTA approach originates from the fact that this approach relies on the smallness of the evolution parameters μ_S [cf. Sec. III B], which decreases with increasing potential depth.

The relative efficiency of the eSTA-based atom transport – compared to its STA-based counterpart – is illustrated by Fig. 6, which depicts the dependence of the time $t_{0.99}$ required to first reach the fidelity of 0.99 on the lattice depth U_0 for the fixed transport distance $d = 85 l_z$. As already established, it can be inferred from this figure that the eSTA method constitutes an improvement of the STA scheme for deeper potentials – in this example for $U_0 \gtrsim 80 E_R$ – because a shorter transport time is needed to reach the same fidelity of 0.99. On the other hand, for more shallow potentials this is not the case. In fact, in a narrow range between $U_0 \sim 65 E_R$ and $U_0 \sim 80 E_R$ eSTA even yields results inferior to that of STA. This outcome – that eSTA does not always result in higher fidelities than

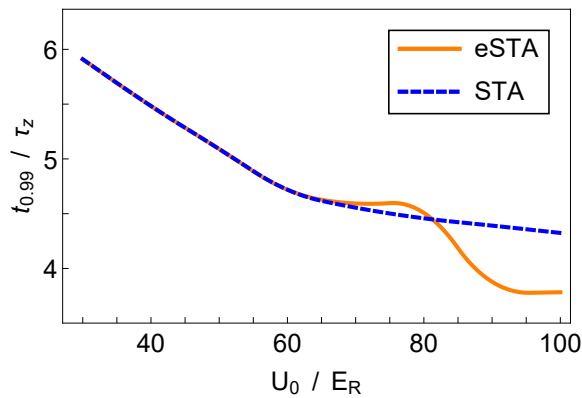


FIG. 6: (Color online) The time $t_{0.99}$ for which a fidelity of 0.99 is first reached for different potential depths U_0 . The transport distance d was set to $85 l_z$, while the transverse beam waists are $w_{x/y,0} = 4.2 \times 10^6 l_z$.

STA – seems to be consistent with the heuristic character of the eSTA approach. However, eSTA is expected to reach perfect fidelity and be an improvement over STA for $\mu_S \rightarrow 0$ [cf. Eq. (14)].

It is pertinent to also comment on the obtained results for the atom-transport fidelity [cf. Figs. 3 – 5] from the point of view of the typical shapes of the corresponding trap-trajectory solutions [cf. Figs. 1 – 2]. What can be inferred is that the typical times t_f needed for a high-fidelity transport correspond to trap-trajectory solutions that do not display oscillatory features. For instance, the eSTA trap trajectory for $t_f/\tau_z = 2$ in Fig. 2(a), which has oscillating character, does not allow for a high-fidelity atom transport. In other words, in the system at hand only non-oscillatory solutions for the trajectory of the moving lattice can enable such transport.

For the sake of completeness, it is worthwhile to briefly discuss the effect of varying transverse beam waists on the efficiency of atomic transport. Our calculations show that the variation of the waists leads to appreciable changes (for fixed values of other relevant parameters) of the fidelity only for rather shallow lattices, i.e. for lattice depths as small as several tens of E_R . For larger lattice depths the results are practically insensitive to the size of the transverse beam waists. This is illustrated in Fig. 7, where the dependence of the fidelity on the transport time is shown for the lattice depths U_0 of 20, 30, and $100 E_R$ with the relevant waists chosen to be $w_{x/y,0} = 300 l_z$. For the parameter choice corresponding to Fig. 7 the behavior of the fidelity changes for lattice depths U_0 just slightly above $30 E_R$ and remains essentially unchanged upon further increase of $w_{x/y,0}$.

B. Comparison to other approaches

In what follows, we complement our analysis of STA and eSTA results for the atom-transport fidelity by comparing these results to those originating from other

known approaches. To be more precise, we consider approaches based on the use of sine-shaped and triangular velocity profiles for the potential path. The time-dependent forms of these two profiles are given by:

$$q_0^s(t) = \frac{v_0}{2} \left[t - \frac{\sin\left(2\pi\frac{t}{t_f}\right)}{2\pi} t_f \right], \quad (34)$$

$$q_0^t(t) = \begin{cases} v_0 t^2/t_f, & \text{for } 0 \leq t \leq t_f/2, \\ v_0 (2t - t_f/2 - t^2/t_f), & \text{for } t_f/2 < t \leq t_f, \end{cases} \quad (35)$$

with the maximal velocity $v_0 = 2d/t_f$.

The approach based on the triangular velocity profile is also known as the *bang-bang* approach [5, 6, 10]. As a consequence of discontinuities in its corresponding acceleration profile, this approach leads to additional motional heating in the regime of fast transport. As a result, it showed a relatively poor performance in some

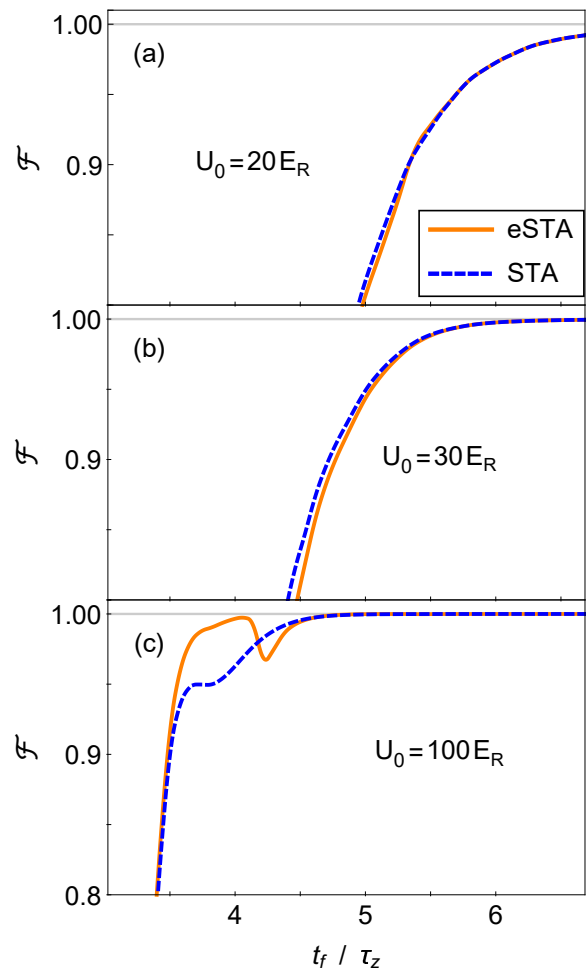


FIG. 7: (Color online) The dependence of the atom-transport fidelity on the transport time t_f , for a lattice depth U_0 of (a) $20 E_R$, (b) $30 E_R$, and (c) $100 E_R$. The transverse beam waists are $w_{x/y,0} = 300 l_z$, while the transport distance is $d = 85 l_z$.

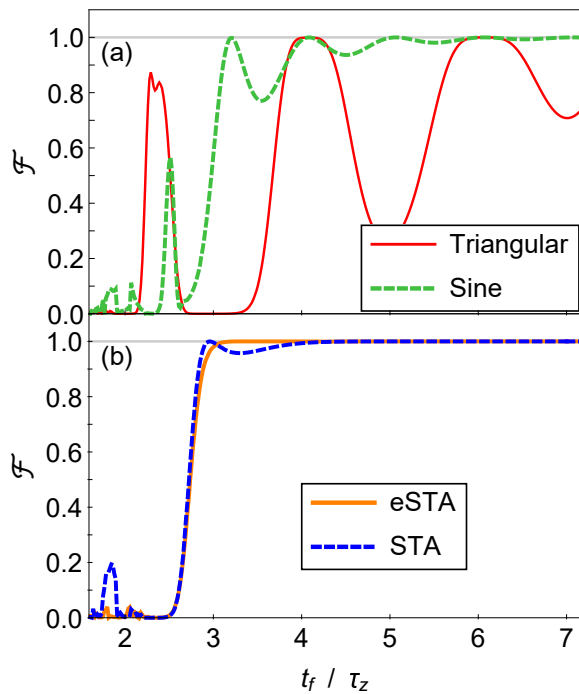


FIG. 8: (Color online) The atom transport fidelity for an atom prepared in the longitudinal motional ground state and moved by a distance $d = 140 l_z$. The results correspond to (a) sine-shaped and triangular velocity profiles and (b) STA and eSTA methods. The lattice depth is set to $U_0 = 2610 E_R$, while the transverse waists are $w_{x,0} = 1790 l_z$ and $w_{y,0} = 537 l_z$.

previous studies, e.g. in Ref. [9]. On the other hand, the sine-shaped profile represent an improvement over the bang-bang approach, since its attendant acceleration is continuous during the entire transport process. However, it is plausible to expect that STA and eSTA approaches should lead to much better results than these pre-selected velocity profiles. Namely, the STA approach is based upon inverse engineering and makes use of the specific form of the Hamiltonian in question to obtain a tailored trap trajectory. Likewise, being based on STA solutions for simplified systems, eSTA solutions inherit this last property of their STA counterparts.

The fidelities obtained using triangular and sine-shaped velocity profiles are compared to those resulting from the application of STA/eSTA methods in Fig. 8. The plot shows the dependence of \mathcal{F} on the transport times t_f for an atom that is initially prepared in the longitudinal motional ground state and moved by a fixed distance (here $d = 140 l_z$), with the target state being the ground state of the displaced OCB potential.

The triangular velocity profile shows strong oscillations in fidelity, a trend that gradually becomes more prominent upon reducing transport times t_f , up until the complete breakdown of the fidelity for $t_f \approx 2.1 \tau_z$ [cf. Fig. 8(a)]. Somewhat better results are obtained for the

sine-shaped velocity profile. Even though the latter also show oscillations, these are much less pronounced than in the triangular case and start for much shorter transport times; the complete breakdown occurs for $t_f \approx 2.3 \tau_z$.

In accordance with the aforementioned expectation, a significant improvement over these previous results is obtained using STA and eSTA, where only one major drop in fidelity takes place for $t_f \approx 2.9 \tau_z$ [cf. Fig. 8(b)]. While eSTA results in smaller fidelities than STA for times $t_f \approx 2.9 \tau_z$ very close to the breakdown point, the eSTA method still leads to slightly larger fidelities than STA for almost all transport times.

VI. SUMMARY AND CONCLUSIONS

In summary, using a combination of advanced analytical and numerical techniques in this paper we investigated fast single-atom transport in moving optical lattices (optical conveyor belts). Unlike previous theoretical studies of fast atomic transport, which were almost exclusively based on simplified scenarios – such as strictly one-dimensional systems and/or purely harmonic trapping potentials – we studied this phenomenon by taking fully into account the three-dimensional, anharmonic trapping potential of the system under consideration.

Our results for atom-transport fidelities – obtained using both STA and eSTA approaches – correspond to realistic values of the relevant system parameters (beam waists, lattice depths, transport distances, etc.). Moreover, our study demonstrates the feasibility of applying the recently proposed eSTA method to a realistic experimental system. It shows that eSTA – envisioned as an improvement of the existing STA techniques – indeed yields more efficient atom transport in optical conveyor belts than STA in a broad range of system parameters.

It can be expected that our present study will motivate further attempts towards realistic modelling of single-atom transport in various optically-trapped atomic systems, such as optical lattices of different geometry [45, 46]. In addition, while in the present work only near-ground state atoms have been considered, it is worthwhile to also investigate the finite-temperature effects (leading, e.g., to finite atom lifetime in traps) and optically-induced heating (due to optical-potential fluctuations). Likewise, this study is of utmost relevance for future experiments in optical conveyor belts. In particular, an experimental corroboration of our results for the atom-transport fidelities is clearly called for.

Acknowledgments

This research was supported by the Deutsche Forschungsgemeinschaft (DFG) – SFB 1119 – 236615297.

Appendix A: Derivation of the expression for G_n

In the following we derive an expression that can be used for the numerical evaluation of the first auxiliary function G_n [cf. Eq. (18)] in our problem. For the sake of brevity, the multi-indices $\mathbf{n} \equiv (n_x, n_y, n_z)$ and $\mathbf{n}_r \equiv (n_x, n_y)$ are used. It should be borne in mind that the main quantum number n of a 3D harmonic oscillator is given by the sum of the quantum numbers of three 1D oscillators, i.e. $n = n_x + n_y + n_z$.

By inserting the transport modes of a 3D harmonic Hamiltonian, written in the coordinate representation, into Eq. (18) we obtain the expression

$$\begin{aligned}
G_{\mathbf{n}} = & - \int_0^{t_f} dt \int_{-\infty}^{\infty} dZ \int_{-\infty}^{\infty} dY \int_{-\infty}^{\infty} dX \frac{\exp[i(\omega_x n_x + \omega_y n_y + \omega_z n_z) t]}{\sqrt{2^n n_x! n_y! n_z! \pi^3}} \\
& \times H_{n_x}(X) H_{n_y}(Y) H_{n_z}[Z_C(t)] \exp(-X^2) \exp(-Y^2) \exp[-Z_C(t)^2] \\
& \times \left(\frac{C P_0 \cos[\sqrt{2} k l_z Z_0(t)]^2}{w_x[Z_0(t)] w_y[Z_0(t)]} \exp \left[-4 \left(\frac{X^2 l_x^2}{w_x[Z_0(t)]^2} + \frac{Y^2 l_y^2}{w_y[Z_0(t)]^2} \right) \right] \right. \\
& \left. + \frac{\hbar}{2} [\omega_x X^2 + \omega_y Y^2 + \omega_z Z_0(t)^2] - U_0 \right), \tag{A1}
\end{aligned}$$

with the dimensionless coordinates $X = x/(l_x \sqrt{2})$, $Y = y/(l_y \sqrt{2})$, $Z = z/(l_z \sqrt{2})$, and new functions $Z_0(t) \equiv Z - q_0(t)/(l_z \sqrt{2})$, $Z_C(t) \equiv Z - q_{c,z}(t)/(l_z \sqrt{2})$. For notational convenience, the waists will hereafter be denoted by $w_{x/y}[Z_0(t)]$, instead of $w_{x/y}[Z_0(t) l_z \sqrt{2}]$. The final expression for $G_{\mathbf{n}}$ will be obtained by treating the different terms and integrations separately from each other.

1. Integration over the transverse directions

We first carry out the integrations in X and Y directions, because those are conceptually easier to do than the Z integration. Therefore, the integral we are considering here is given by

$$\begin{aligned}
\mathbb{I}_{r,2}^{\mathbf{n}_r}[Z_0(t)] = & \int_{-\infty}^{\infty} dY \int_{-\infty}^{\infty} dX H_{n_x}(X) H_{n_y}(Y) \exp(-X^2) \exp(-Y^2) \\
& \times \left(A[Z_0(t)] \exp \left[-4 \left(\frac{X^2 l_x^2}{w_x[Z_0(t)]^2} + \frac{Y^2 l_y^2}{w_y[Z_0(t)]^2} \right) \right] \right. \\
& \left. + \frac{\hbar}{2} [\omega_x X^2 + \omega_y Y^2 + \omega_z Z_0(t)^2] - U_0 \right), \tag{A2}
\end{aligned}$$

with $A(Z) = C P_0 \cos^2(k l_z Z) / [w_x(Z) w_y(Z)]$ and $U_0 = C P_0 / (w_{x,0} w_{y,0})$. Using the orthogonality and the recurrence relation of Hermite polynomials [47]

$$\int_{-\infty}^{\infty} dx H_m(x) H_l(x) \exp(-x^2) = \sqrt{\pi} 2^m m! \delta_{l,m}, \tag{A3}$$

$$x H_m(x) = \frac{1}{2} H_{m+1}(x) + m H_{m-1}(x), \tag{A4}$$

the X -integration of the second term in Eq. (A2) can readily be carried out. It yields the following result:

$$\begin{aligned}
\mathbb{I}_{r,2}^{n_x}[Z_0(t)] = & \frac{\hbar}{2} \int_{-\infty}^{\infty} dX \left[\omega_x X^2 + \omega_y Y^2 + \omega_z^2 Z_0(t)^2 - \frac{2U_0}{\hbar} \right] H_{n_x}(X) \exp(-X^2) \\
= & \frac{\hbar \omega_x}{4} \sqrt{\pi} (\delta_{n_x,0} + 4 \delta_{n_x,2}) + \sqrt{\pi} \frac{\hbar}{2} \left[\omega_y Y^2 + \omega_z Z_0(t)^2 - \frac{2U_0}{\hbar} \right] \delta_{n_x,0}. \tag{A5}
\end{aligned}$$

Owing to the symmetry of the problem, the Y -integration of Eq. (A5) is conceptually equivalent to the X -integration. Therefore, we just state the final result for the integrated second term [cf. Eq. (A2)]:

$$\begin{aligned}
\mathbb{I}_{r,2}^{\mathbf{n}_r}[Z_0(t)] = & \pi \frac{\hbar}{2} \omega_z Z_0(t)^2 \delta_{n_x,0} \delta_{n_y,0} \\
& + \pi \hbar \left[\left(\frac{\omega_x + \omega_y}{4} - \frac{U_0}{\hbar} \right) \delta_{n_x,0} \delta_{n_y,0} + \omega_x \delta_{n_x,2} \delta_{n_y,0} + \omega_y \delta_{n_x,0} \delta_{n_y,2} \right]. \tag{A6}
\end{aligned}$$

Let us now focus on the first term in Eq. (A2). We can restrict our calculations to the integration of

$$I_{x,1}^{n_x} [Z_0(t)] = \int_{-\infty}^{\infty} dX H_{n_x}(X) \exp(-X^2) \exp\left(-4 \frac{X^2 l_x^2}{w_x [Z_0(t)]^2}\right). \quad (\text{A7})$$

As a consequence of the presence of the second exponential in the last integral, we cannot simply use the orthogonality relation (A3) of Hermite polynomials to evaluate it. However, this integral can be computed using the formula of Faà di Bruno [48] for Hermite polynomials

$$H_m(x) = (-1)^m \sum_{k_1+2k_2=m} \frac{m!}{k_1!k_2!} (-1)^{k_1+k_2} (2x)^{k_1}. \quad (\text{A8})$$

In addition, we make use of the identity

$$\int_{-\infty}^{\infty} dx x^n \exp(-ax^2 + bx + c) = \exp\left(\frac{b^2}{4a} + c\right) \sum_{k=0}^{\lfloor n/2 \rfloor} \binom{n}{2k} \left(\frac{b}{2a}\right)^{n-2k} \frac{\Gamma(k+1/2)}{a^{k+1/2}}, \quad (\text{A9})$$

where $\Gamma(x)$ is the gamma function. Putting everything together, the following result is finally obtained:

$$\begin{aligned} I_{x,1}^{n_x} [Z_0(t)] &= \sum_{k_1+2k_2=n_x} \frac{n_x!}{k_1!k_2!} (-1)^{n_x+k_1+k_2} \int_{-\infty}^{\infty} dX (2X)^{k_1} \exp(-X^2) \exp\left(-4 \frac{X^2 l_x^2}{w_x [Z_0(t)]^2}\right) \\ &= \sum_{\substack{k_1+2k_2=n_x \\ k_1 \text{ even}}} \frac{n_x!}{k_1!k_2!} (-1)^{k_2} \Gamma\left(\frac{k_1+1}{2}\right). \end{aligned} \quad (\text{A10})$$

In the last step we made use of the fact that the integral in Eq. (A7) is equal to zero for odd values of n_x due to the symmetry of the integrand. Similar result can also be obtained for the Y -integration. Thus, the final integrated form for the first term in Eq. (A2), up to the Z -dependent factor $A[Z_0(t)]$, is given by

$$\begin{aligned} I_{r,1}^{\mathbf{n}} [Z_0(t)] &= \sum_{\substack{k_1+2\tilde{k}_2=n_x \\ k_1 \text{ even}}} \sum_{\substack{\tilde{k}_1+2\tilde{k}_2=n_y \\ \tilde{k}_1 \text{ even}}} \frac{n_x! n_y!}{k_1!k_2! \tilde{k}_1! \tilde{k}_2!} (-1)^{k_2+\tilde{k}_2} 2^{k_1+\tilde{k}_1} \left(\frac{w_x [Z_0(t)]^2}{4l_x^2 + w_x [Z_0(t)]^2}\right)^{\frac{k_1+1}{2}} \\ &\quad \times \Gamma\left(\frac{k_1+1}{2}\right) \Gamma\left(\frac{\tilde{k}_1+1}{2}\right) \left(\frac{w_y [Z_0(t)]^2}{4l_y^2 + w_y [Z_0(t)]^2}\right)^{\frac{\tilde{k}_1+1}{2}}. \end{aligned} \quad (\text{A11})$$

2. Integration over the longitudinal direction

The most general form we can obtain for $G_{\mathbf{n}}$ after the integrations over the X - and Y coordinates is given by

$$\begin{aligned} G_{\mathbf{n}} &= - \int_0^{t_f} dt \int_{-\infty}^{\infty} dZ \frac{\exp[i(\omega_x n_x + \omega_y n_y + \omega_z n_z) t]}{\sqrt{2^n n_x! n_y! n_z! \pi}} \\ &\quad \times H_{n_z} [Z_C(t)] \exp[-Z_C(t)^2] \left(\frac{1}{\pi} A[Z_0(t)] I_{r,1}^{\mathbf{n}_r} [Z_0(t)] + \frac{\hbar}{2} \omega_z Z_0(t)^2 \delta_{n_x,0} \delta_{n_y,0} \right. \\ &\quad \left. + \hbar \left[\left(\frac{\omega_x + \omega_y}{4} - \frac{U_0}{\hbar} \right) \delta_{n_x,0} \delta_{n_y,0} + \omega_x \delta_{n_x,2} \delta_{n_y,0} + \omega_y \delta_{n_x,0} \delta_{n_y,2} \right] \right). \end{aligned} \quad (\text{A12})$$

For the Z -integration we treat the three terms in the brackets of Eq. (A12) independently.

The integration of the third term is conceptually the simplest one and is thus treated first. The integral we need to evaluate has the form

$$I_{z,3}^{\mathbf{n}} = B^{\mathbf{n}_r} \int_{-\infty}^{\infty} dz (l_z \sqrt{2})^{-1} H_{n_z} [Z_C(t)] \exp[-Z_C(t)^2], \quad (\text{A13})$$

where we have set $B^{\text{nr}} \equiv \hbar [(\omega_x/4 + \omega_y/4 - U_0/\hbar) \delta_{n_x,0} \delta_{n_y,0} + \omega_x \delta_{n_x,2} \delta_{n_y,0} + \omega_y \delta_{n_x,0} \delta_{n_y,2}]$.

Since we want to use orthogonality relation (A3), we have to rewrite the Hermite polynomial and the exponential function such that their arguments become independent of $q_0(t)$ and $q_{c,z}(t)$. We can accomplish this using the relations of the generating function of Hermite polynomials and the following sum representation [47]

$$\exp(2xt - t^2) = \sum_{m=0}^{\infty} \frac{H_m(x)t^m}{m!}, \quad (\text{A14})$$

$$H_m(x+y) = \sum_{k=0}^m \binom{m}{k} H_k(x) (2y)^{m-k}. \quad (\text{A15})$$

We are now able to calculate the integral and obtain the following

$$\begin{aligned} \mathbb{I}_{z,3}^{\text{n}} &= B^{\text{nr}} \int_{-\infty}^{\infty} dZ \sum_{k=0}^{n_z} \binom{n_z}{k} H_k(Z) \left[-\sqrt{2} \frac{q_{c,z}(t)}{l_z} \right]^{n_z-k} \\ &\quad \times \exp(-Z^2) \sum_{m=0}^{\infty} \frac{H_m(Z)}{m!} \left[\frac{q_{c,z}(t)}{\sqrt{2} l_z} \right]^m \\ &= B^{\text{nr}} \sqrt{\pi} \left[\sqrt{2} \frac{q_{c,z}(t)}{l_z} \right]^{n_z} \sum_{k=0}^{n_z} \binom{n_z}{k} (-1)^{n_z-k}. \end{aligned} \quad (\text{A16})$$

The last line of Eq. (A16) vanishes for any value of n_z except for $n_z = 0$, which can be seen by making use of the binomial theorem. Hence, the solution to the first integral in Z is given by the simple form

$$\mathbb{I}_{z,3}^{\text{n}} = B^{\text{nr}} \sqrt{\pi} \delta_{n_z,0}. \quad (\text{A17})$$

The Z -integration of the second term of Eq. (A12) can be carried out by combining the above integration steps and using relation (A4). Thus, the second integral in Z is given by

$$\begin{aligned} \mathbb{I}_{z,2}^{\text{n}}(t) &= \frac{\hbar}{2} \omega_z \int_{-\infty}^{\infty} dZ \exp[-Z_C(t)^2] Z_0(t)^2 H_{n_z}[Z_C(t)] \delta_{n_x,0} \delta_{n_y,0} \\ &= \frac{\hbar}{2} \omega_z \int_{-\infty}^{\infty} dZ \sum_{m=0}^{\infty} \frac{1}{m!} \left[\frac{q_{c,z}(t)}{\sqrt{2} l_z} \right]^m \exp[-Z^2] \delta_{n_x,0} \delta_{n_y,0} \left[\frac{1}{4} H_{m+2}(Z) \right. \\ &\quad \left. + \left(m + \frac{1}{2}\right) H_m(Z) + m(m-1) H_{m-2}(Z) + \frac{q_0(t)^2}{2 l_z^2} H_m(Z) \right. \\ &\quad \left. - \sqrt{2} \frac{q_0(t)}{l_z} \left[\frac{1}{2} H_{m+1}(Z) + m H_{m-1}(Z) \right] \right] \sum_{l=0}^{n_z} \binom{n_z}{l} H_l(Z) \left[-\sqrt{2} \frac{q_{c,z}(t)}{l_z} \right]^{n_z-l} \\ &= \frac{\hbar}{2} \sqrt{\pi} \omega_z \delta_{n_x,0} \delta_{n_y,0} \left[\sqrt{2} \frac{q_{c,z}(t)}{l_z} \right]^{n_z} \sum_{l=0}^{n_z} \binom{n_z}{l} (-1)^{n_z-l} \left[\frac{l(l-1)}{2} \left[\frac{q_{c,z}(t)}{l_z} \right]^{-2} - l \frac{q_0(t)}{q_{c,z}(t)} + l \right], \end{aligned} \quad (\text{A18})$$

In the last step we utilized the orthogonality of Hermite polynomials [cf. Eq. (A3)], the binomial theorem and the general condition $n > 0$. Using mathematical induction, we can further simplify this last result and obtain the following form:

$$\mathbb{I}_{z,2}^{\text{n}}(t) = \frac{\hbar \omega_z}{\sqrt{2} l_z} \sqrt{\pi} \delta_{n_x,0} \delta_{n_y,0} \left(\delta_{n_z,1} [q_{c,z}(t) - q_0(t)] + \delta_{n_z,2} \right). \quad (\text{A19})$$

This shows that the only nonvanishing contributions are those with $n_z = 1, 2$.

The last integral that we have to compute corresponds to the first term in Eq. (A12) and has the form

$$\mathbb{I}_{z,1}^{\text{n}}(t) = \frac{C P_0}{\pi} \int_{-\infty}^{\infty} dZ \frac{I_{r,1}^{\text{nr}}[Z_0(t)] H_{n_z}[Z_C(t)] \exp[-Z_C(t)^2]}{w_x[Z_0(t)] w_y[Z_0(t)]} \cos^2 \left[\sqrt{2} k l_z Z_0(t) \right]. \quad (\text{A20})$$

The dependence of the denominator on Z makes it impossible to find an analytical solution for the above integral even for concrete values of n_z . Therefore, as part of our optimization procedure, we perform numerical evaluation of this integral.

Putting the results of the last two subsections together, we obtain the integrated form of $G_{\mathbf{n}}$:

$$G_{\mathbf{n}} = - \int_0^{t_f} dt \frac{\exp[i(\omega_x n_x + \omega_y n_y + \omega_z n_z) t]}{\sqrt{2^n n_x! n_y! n_z!}} \times \left[\hbar \delta_{n_z,0} (\omega_x \delta_{n_x,2} \delta_{n_y,0} + \omega_y \delta_{n_x,0} \delta_{n_y,2}) + \frac{1}{\sqrt{\pi}} \mathbf{I}_{z,2}^{\mathbf{n}}(t) + \frac{1}{\sqrt{\pi}} \mathbf{I}_{z,1}^{\mathbf{n}}(t) \right]. \quad (\text{A21})$$

Because an analytic solution for $\mathbf{I}_{z,1}^{\mathbf{n}}(t)$ does not exist, this integral can only be computed numerically.

3. Approximation for $G_{\mathbf{n}}$

Because the numerical evaluation of two-dimensional integrals can be rather time-consuming, we simplify the z -dependent denominator within the function $\mathbf{I}_{z,1}^{\mathbf{n}}(t)$. By analyzing the exponential function in Eq. (A20), we see that the main contributions of $\mathbf{I}_{z,1}^{\mathbf{n}}(t)$ are localized around the classical path of the particle $q_{c,z}(t)$. Thus, we will first express the argument of the z -dependent denominator in terms of $q_{c,z}(t)$, resulting in

$$\begin{aligned} \sqrt{2} Z_0(t) l_z &= q_{c,z}(t) + |\ddot{q}_{c,z}(t)/\omega_z^2| \leq q_{c,z}(t) + \frac{\ddot{q}_{c,z}^{\max}}{\omega_z^2} \\ &\approx q_{c,z}(t) + \frac{10d}{t_f^2 \omega_z^2} \leq q_{c,z}(t) + \frac{1}{\sqrt{2}} \tilde{U}^{7/4} l_z. \end{aligned} \quad (\text{A22})$$

It should be borne in mind that within the STA solution, the acceleration of the particle $\ddot{q}_{c,z}(t)$ is connected to the difference in classical particle and potential paths [cf. Eq. (11)]. Moreover, in the second line the following inequality for the particle acceleration was used:

$$\ddot{q}_{c,z}^{\max} := \max_{t \in [0, t_f]} \ddot{q}_{c,z}(t) = \frac{d}{t_f^2} \tilde{a} \leq |a_{\max}| = \frac{1}{\sqrt{2}} \tilde{U}^{7/4} \frac{l_z}{\omega_z^{-2}}, \quad (\text{A23})$$

where the dimensionless lattice depth $\tilde{U} \equiv U_0/E_R$ was introduced. In Eq. (A23) $|a_{\max}|$ is the maximal acceleration of the trap (i.e., that of the moving OCB potential), while the dimensionless parameter \tilde{a} is the maximal acceleration of an atom in the trap expressed in units of d/t_f^2 . As already stated in Sec. V A, the upper bound for \tilde{a} is close to 10, more precisely 9.372, while the lower bound equals 2 [5].

Now, let us examine the Rayleigh lengths by looking at the following expression

$$\begin{aligned} \frac{Z_{R,x/y}}{\sqrt{2} l_z} &= \left[\frac{m^2 U_0}{\hbar^2 m} \left(\frac{1}{Z_{R,x}^2} + \frac{1}{Z_{R,y}^2} + 2k^2 \right) \right]^{1/4} Z_{R,x/y} \\ &\gg \left(\frac{U_0 m}{\hbar^2} 4k^2 \right)^{1/4} k^{-1} = (2\tilde{U})^{1/4}, \end{aligned} \quad (\text{A24})$$

with the characteristic length-scale $l_z = \sqrt{\hbar/(2m\omega_z)}$, the frequency $\omega_z = \sqrt{U_0 (Z_{R,x}^{-2} + Z_{R,y}^{-2} + 2k^2)}/m$ and the recoil energy $E_R = \hbar^2 k^2/(2m)$.

Furthermore, we used the paraxial approximation $Z_{R,x/y} \gg 1/k$ in the second line, which is also used to derive the potential for a Gaussian laser beam and, subsequently, an OCB. Hence, the paraxial approximation is always fulfilled for these types of potentials. Furthermore, we are concerned with the regime in which our lattice depth is at least several E_R , resulting in $\tilde{U} > 1$ and thus $Z_{R,x/y} l_z^{-1} \gg 1$.

Putting everything together shows that the regime of the numerator of inequality (A22) is of the same order of magnitude as that of the last equality in (A24), resulting in

$$\frac{\sqrt{2} Z_0(t) l_z}{Z_{R,x}} \lesssim \frac{q_{c,z}(t)}{Z_{R,x}} + \frac{\frac{1}{\sqrt{2}} \tilde{U}^{7/4} l_z}{Z_{R,x}} \approx \frac{q_{c,z}(t)}{Z_{R,x}} \quad (\text{A25})$$

Now, scales on which the approximated denominator and the exponential function change significantly can be compared. Using inequality (A24), we conclude that the influence of changes in the denominator is negligible small

on the scales on which the exponential functions drops significantly, resulting in the central approximation

$$\sqrt{1 + \left[\frac{\sqrt{2} Z_0(t) l_z}{Z_{R,x/y}} \right]^2} \approx 1. \quad (\text{A26})$$

Using once again Faà di Bruno's representation for Hermite polynomials [cf. Eq. (A8)] and this last approximation, together with Euler's formula for the cosine function and integral relation (A9), Eq. (A20) adopts the approximated form:

$$\Gamma_{z,1}^{\mathbf{n},ap.}(t) = \frac{U_0}{4\pi} \Gamma_{r,1}^{\mathbf{n}_r}(0) \sum_{k_1+2k_2=n_z} (-1)^{n_z+k_1+k_2} \frac{n_z!}{k_1!k_2!} 2^{k_1} \sum_{l=0}^{k_1} \binom{k_1}{l} \left[-\frac{q_{c,z}(t)}{\sqrt{2} l_z} \right]^{k_1-l} D(l). \quad (\text{A27})$$

For the sake of readability, we introduced the auxiliary function

$$\begin{aligned} D(l) = & \sum_{\lambda=0}^{\lfloor l/2 \rfloor} \binom{l}{2\lambda} \Gamma(\lambda + 1/2) \left[2 \left[\frac{q_{c,z}(t)}{\sqrt{2} l_z} \right]^{l-2\lambda} \right. \\ & + \exp(-2k^2 l_z^2) \exp\left(+ 2ik [q_{c,z}(t) - q_0(t)] \right) \left[\frac{q_{c,z}(t)}{\sqrt{2} l_z} + i\sqrt{2} k l_z \right]^{l-2\lambda} \\ & \left. + \exp(-2k^2 l_z^2) \exp\left(- 2ik [q_{c,z}(t) - q_0(t)] \right) \left[\frac{q_{c,z}(t)}{\sqrt{2} l_z} - i\sqrt{2} k l_z \right]^{l-2\lambda} \right]. \end{aligned} \quad (\text{A28})$$

Thus, we have reduced the calculation of $G_{\mathbf{n}}$ to the numerical evaluation a one-dimensional integral in the time domain. The relative difference between the results of the full numerical integration and our approximated solutions was verified to be of the order of 10^{-5} . At the same time, our approximate numerical integration is around 15 times faster than obtaining the numerically-exact solution.

Appendix B: Derivation of the expression for \mathbf{K}_n

Here we are concerned with the calculation of $\mathbf{K}_{\mathbf{n}}$. To begin with, the gradient of H_S with respect to λ was computed. Use has also been made of the fact that the substitution $q_0(\boldsymbol{\lambda}; t) = q_0(\boldsymbol{\lambda}_0; t) + f(\boldsymbol{\alpha}; t)$ implies that

$$\nabla_{\lambda} q_0(\boldsymbol{\lambda}; t) = \nabla_{\alpha} f(\boldsymbol{\alpha}; t). \quad (\text{B1})$$

By inserting the transport modes of the 3D harmonic oscillator, written in the coordinate representation, into Eq. (20), we obtain

$$\begin{aligned} \mathbf{K}_{\mathbf{n}} = & \int_0^{t_f} dt \int_{-\infty}^{\infty} dZ \int_{-\infty}^{\infty} dY \int_{-\infty}^{\infty} dX \frac{-\nabla_{\alpha} f(\boldsymbol{\alpha}; t)}{\sqrt{2^n n_x! n_y! n_z! \pi^3}} \exp[i(n_x \omega_x + n_y \omega_y + n_z \omega_z) t] \\ & \times \frac{C P_0}{w_x [Z_0(t)] w_y [Z_0(t)]} H_{n_x}(X) H_{n_y}(Y) H_{n_z}[Z_C(t)] \exp[-X^2 - Y^2 - Z_C(t)^2] \\ & \times \exp \left[-4 \left(\frac{X^2 l_x^2}{w_x [Z_0(t)]^2} + \frac{Y^2 l_y^2}{w_y [Z_0(t)]^2} \right) \right] \left(k \sin \left[2^{3/2} k l_z Z_0(t) \right] + \frac{Z_0(t)}{2^{5/2} l_z^3} \left(\cos \left[2^{3/2} k l_z Z_0(t) \right] + 1 \right) \right) \\ & \times \left[\left(1 - \frac{8X^2 l_x^2}{w_x [Z_0(t)]^2} \right) \left(\frac{Z_{R,x}}{\frac{Z_{R,x}^2}{2l_z^2} + Z_0(t)^2} \right)^2 + \left(1 - \frac{8Y^2 l_y^2}{w_y [Z_0(t)]^2} \right) \left(\frac{Z_{R,y}}{\frac{Z_{R,y}^2}{2l_z^2} + Z_0(t)^2} \right)^2 \right]. \end{aligned} \quad (\text{B2})$$

1. Integration over the transverse directions

By analogy to what was done in Sec. A1, we first treat the integration in X and Y . In other words, we are considering the integral

$$\begin{aligned} \tilde{\mathbf{I}}_r^{\mathbf{n}_r} [Z_0(t)] &= \int_{-\infty}^{\infty} dY \int_{-\infty}^{\infty} dX \exp(-X^2 - Y^2) \exp \left[-4 \left(\frac{X^2 l_x^2}{w_x [Z_0(t)]^2} + \frac{Y^2 l_y^2}{w_y [Z_0(t)]^2} \right) \right] \\ &\times \mathbf{H}_{n_x}(X) \mathbf{H}_{n_y}(Y) \left(k \sin \left[2^{3/2} k l_z Z_0(t) \right] + \frac{Z_0(t)}{2^{5/2} l_z^3} \left[\cos \left(2^{3/2} k l_z Z_0(t) \right) + 1 \right] \right) \\ &\times \left[\left(\frac{Z_{R,x}}{\frac{Z_{R,x}^2}{2l_x^2} + Z_0(t)^2} \right)^2 \left(1 - \frac{8X^2 l_x^2}{w_x [Z_0(t)]^2} \right) + \left(\frac{Z_{R,y}}{\frac{Z_{R,y}^2}{2l_y^2} + Z_0(t)^2} \right)^2 \left(1 - \frac{8Y^2 l_y^2}{w_y [Z_0(t)]^2} \right) \right]. \end{aligned} \quad (\text{B3})$$

The integrations in X and Y are conceptually the same and somewhat similar to what was done in previous sections. As a consequence, the first term can readily be obtained using previous results:

$$\tilde{\mathbf{I}}_{r,1}^{\mathbf{n}_r} [Z_0(t)] = k \sin \left[2^{3/2} k l_z Z_0(t) \right] \mathbf{I}_{r,1}^{\mathbf{n}_r} [Z_0(t)]. \quad (\text{B4})$$

The second integral is given by

$$\begin{aligned} \tilde{\mathbf{I}}_{r,2,x}^{\mathbf{n}_r} [Z_0(t)] &= \int_{-\infty}^{\infty} dX X^2 \mathbf{H}_{n_x}(X) \exp(-X^2) \exp \left(-4 \frac{X^2 l_x^2}{w_x [Z_0(t)]^2} \right) \\ &= \sum_{\substack{k_1+2k_2=n_x \\ k_1 \text{ even}}} \frac{n_x!}{k_1!k_2!} (-1)^{k_2} 2^{k_1} \left(\frac{w_x [Z_0(t)]^2}{4l_x^2 + w_x [Z_0(t)]^2} \right)^{\frac{k_1+3}{2}} \Gamma \left(\frac{k_1+3}{2} \right). \end{aligned} \quad (\text{B5})$$

where we made use of integral relation (A9) and Faá di Bruno's representation of Hermite polynomials (A8). It should be stressed that Eq. (B6) is equal to zero for odd n_x due to the symmetry of the integral, akin to the X -integration for $G_{\mathbf{n}}$ [cf. Eq. (A10)]. The Y -integration entails similar steps. Putting it all together, the full form of the second term of Eq. (B2) reads

$$\begin{aligned} \tilde{\mathbf{I}}_{r,2}^{\mathbf{n}_r} [Z_0(t)] &= - \sum_{i \in \{x,y\}} C_i [Z_0(t)] \frac{2^{3/2} Z_0(t) l_z l_i^2}{w_i [Z_0(t)]^2 \sqrt{\pi}} \mathbf{I}_{r,1}^{0,n_i} [Z_0(t)] \\ &\times \sum_{\substack{k_1+2k_2=n_i \\ k_1 \text{ even}}} (-1)^{k_2} \frac{n_i!}{k_1!k_2!} 2^{k_1+2} \Gamma \left(\frac{k_1+3}{2} \right) \left(\frac{w_i [Z_0(t)]^2}{4l_i^2 + w_i [Z_0(t)]^2} \right)^{\frac{k_1}{2}+1} \\ &+ \left(C_x [Z_0(t)] + C_y [Z_0(t)] \right) \mathbf{I}_{r,1}^{\mathbf{n}_r} [Z_0(t)], \end{aligned} \quad (\text{B6})$$

with the factors

$$C_i(Z) = \frac{1}{8l_z^4} \left[\cos \left(2^{3/2} k l_z Z \right) + 1 \right] \left(\frac{Z_{R,i}}{\frac{Z_{R,i}^2}{2l_i^2} + Z^2} \right)^2. \quad (\text{B7})$$

It should be stressed that the expressions for $\tilde{\mathbf{I}}_{r,1}^{\mathbf{n}_r}$ and $\tilde{\mathbf{I}}_{r,2}^{\mathbf{n}_r}$ are only valid for even values of n_x and n_y , otherwise they are equal to zero.

2. Integration over the longitudinal direction

The most general form we can obtain without approximation of the integrand for \mathbf{K}_n is given by

$$\begin{aligned} \mathbf{K}_n = & - \int_0^{t_f} dt \int_{-\infty}^{\infty} dZ \frac{U_0}{\sqrt{2^n n_x! n_y! n_z! \pi^3}} \exp[i(n_x \omega_x + n_y \omega_y + n_z \omega_z) t] \nabla_{\alpha} f(\boldsymbol{\alpha}; t) \\ & \times \frac{H_{n_z}[Z_C(t)] \exp[-Z_C(t)^2]}{\sqrt{1 + \left[\frac{\sqrt{2} Z_0(t) l_z}{Z_{R,x}}\right]^2} \sqrt{1 + \left[\frac{\sqrt{2} Z_0(t) l_z}{Z_{R,y}}\right]^2}} \left(k \sin\left[2^{3/2} k l_z Z_0(t)\right] \mathbf{I}_{r,1}^{n_r}[Z_0(t)] + \tilde{\mathbf{I}}_{r,2}^{n_r}[Z_0(t)] \right). \end{aligned} \quad (\text{B8})$$

Hence, we need to evaluate the following integral in the Z direction:

$$\tilde{\mathbf{I}}_z^n(t) = - \int_{-\infty}^{\infty} \frac{dZ H_{n_z}[Z_C(t)] \exp[-Z_C(t)^2]}{\sqrt{1 + \left[\frac{\sqrt{2} Z_0(t) l_z}{Z_{R,x}}\right]^2} \sqrt{1 + \left[\frac{\sqrt{2} Z_0(t) l_z}{Z_{R,y}}\right]^2}} \left(k \sin\left[2^{3/2} k l_z Z_0(t)\right] \mathbf{I}_{r,1}^{n_r}[Z_0(t)] + \tilde{\mathbf{I}}_{r,2}^{n_r}[Z_0(t)] \right). \quad (\text{B9})$$

While this integral cannot be computed analytically, we are able to approximate it.

The same procedure to obtain an approximate solution for the Z integral in the first auxiliary function G_n can be used to find an approximate result for the integration of Eq. (B9). Repeating the same steps – that is, approximation of the z -dependent denominator – using the Euler formula and the Faà di Bruno representation for Hermite polynomials [cf. Eq. (A8)], we obtain the final form for the first term

$$\begin{aligned} \tilde{\mathbf{I}}_{z,1}^{n,ap.}(t) = & \frac{ik}{2} \mathbf{I}_{r,1}^{n_r}(0) \exp(-2k^2 l_z^2) \sum_{k_1+2k_2=n_z} \frac{2^{k_1} n_z!}{k_1! k_2!} (-1)^{n_z+k_1+k_2+1} \sum_{l=0}^{k_1} \binom{k_1}{l} \\ & \times \left[-\frac{q_{c,z}(t)}{\sqrt{2} l_z} \right]^{k_1-l} \sum_{\lambda}^{\lfloor l/2 \rfloor} \left[\exp(2ik[q_{c,z}(t) - q_0(t)]) \left[\frac{q_{c,z}(t)}{\sqrt{2} l_z} + i\sqrt{2} k l_z \right]^{l-2\lambda} \right. \\ & \left. - \exp(-2ik[q_{c,z}(t) - q_0(t)]) \left[\frac{q_{c,z}(t)}{\sqrt{2} l_z} - i\sqrt{2} k l_z \right]^{l-2\lambda} \right] \binom{l}{2\lambda} \Gamma(\lambda + 1/2) \end{aligned} \quad (\text{B10})$$

and the second term of Eq. B9.

$$\begin{aligned} \tilde{\mathbf{I}}_{z,2}^{n,ap.}(t) = & - \sum_{i \in \{x,y\}} \frac{2l_i^2}{Z_{R,i}^2 w_{i,0}^2 \sqrt{\pi}} \mathbf{I}_{r,1}^{0,n_i}(0) \sum_{\substack{k_1+2k_2=n_i \\ k_1 \text{ even}}} (-1)^{k_2} \frac{n_i!}{k_1! k_2!} 2^{k_1+2} \Gamma\left(\frac{k_1+3}{2}\right) \\ & \times \left(\frac{w_{i,0}^2}{4l_i^2 + w_{i,0}^2} \right)^{\frac{k_1}{2}+1} \left(\sum_{\tilde{k}_1+2\tilde{k}_2=n_z} \frac{n_z!}{\tilde{k}_1! \tilde{k}_2!} (-1)^{n_z+\tilde{k}_1+\tilde{k}_2} 2^{\tilde{k}_1-1} \sum_{l=0}^{\tilde{k}_1} \left[-\frac{q_{c,z}(t)}{\sqrt{2} l_z} \right]^{\tilde{k}_1-l} \right. \\ & \left. \times \binom{\tilde{k}_1}{l} \left[D(l+1) - \frac{q_0(t)}{\sqrt{2} l_z} D(l) \right] \right) + \left(\frac{1}{Z_{R,x}^2} + \frac{1}{Z_{R,y}^2} \right) \mathbf{I}_{z,1}^{n,ap.}(0) \mathbf{I}_{r,1}^{n_r}(0). \end{aligned} \quad (\text{B11})$$

The computational speedup and the accuracy of the final result are of the same order as in the aforementioned approximation for G_n [cf. Sec. A3].

Appendix C: Parameters of the auxiliary function $f(\boldsymbol{\alpha}; t)$

The values of the parameters $\tilde{a}_{n,k}$ in Eq. (24), rounded to the accuracy of 10^{-8} , are listed in Table I.

$n \backslash k$	1	2	3	4	5	6
3	3268.0278	-1764.7350	1361.6782	-1021.2587	705.894 00	-544.671 30
4	-42 974.565	29 382.838	-24 260.567	18 791.160	-13 235.513	10 339.677
5	238 311.85	-188 292.32	168 031.09	-135 594.78	97 923.184	-77 792.678
6	-731 080.51	636 579.13	-607 620.55	512 478.95	-381 148.45	309 119.12
7	1 362 055.0	-1 270 967.0	1 282 059.8	-1 128 042.6	865 989.78	-719 297.45
8	-1 583 096.2	1 555 055.1	-1 640 810.9	1 500 138.2	-1 188 990.2	1 013 733.1
9	1 124 047.2	-1 148 396.4	1 257 158.1	-1 189 045.8	971 849.37	-851 598.11
10	-446 816.56	470 792.08	-531 275.79	517 653.33	-435 482.68	392 326.73
11	76 285.754	-82 388.614	95 357.192	-95 357.192	82 388.614	-76 285.754

TABLE I: Approximated parameters $\tilde{a}_{n,k}$ for Eq. (24). The relative differences between approximated and exact values are of the order of 10^{-8} . For $n < 3$ the parameter $\tilde{a}_{n,k}$ is equal to zero.

-
- [1] A. Couvert, T. Kawalec, G. Reinaudi, and D. Guéry-Odelin, *Europhys. Lett.* **83**, 13001 (2008).
- [2] M. Murphy, L. Jiang, N. Khaneja, and T. Calarco, *Phys. Rev. A* **79**, 020301(R) (2009).
- [3] S. Masuda and K. Nakamura, *Proc. R. Soc. A* **466**, 1135 (2010).
- [4] D. Chen, H. Zhang, X. Xu, T. Li, and Y. Wang, *Appl. Phys. Lett.* **96**, 134103 (2010).
- [5] E. Torrontegui, S. Ibañez, X. Chen, A. Ruschhaupt, D. Guéry-Odelin, and J. G. Muga, *Phys. Rev. A* **83**, 013415 (2011).
- [6] X. Chen, E. Torrontegui, D. Stefanatos, J.-S. Li, and J. G. Muga, *Phys. Rev. A* **84**, 043415 (2011).
- [7] G. Ness, C. Shkedorov, Y. Florshaim, and Y. Sagi, *New J. Phys.* **20**, 095002 (2018).
- [8] S. Amri, R. Corgier, D. Sugny, E. M. Rasel, N. Gaaloul, and E. Charron, *Sci. Rep.* **9**, 5346 (2019).
- [9] G. T. Hickman and M. Saffman, *Phys. Rev. A* **101**, 063411 (2020).
- [10] Y. Ding, T.-Y. Huang, K. Paul, M. Hao, and X. Chen, *Phys. Rev. A* **101**, 063410 (2020).
- [11] M. R. Lam, N. Peter, T. Groh, W. Alt, C. Robens, D. Meschede, A. Negretti, S. Montangero, T. Calarco, and A. Alberti, *Phys. Rev. X* **11**, 011035 (2021).
- [12] P. Navez, S. Pandey, H. Mas, K. Poullos, T. Fernholz, and W. von Klitzing, *New J. Phys.* **18**, 075014 (2016).
- [13] A. Rodriguez-Prieto, S. Martínez-Garaot, I. Lizuain, and J. G. Muga, *Phys. Rev. Research* **2**, 023328 (2020).
- [14] M. Ebert, A. Gill, M. Gibbons, X. Zhang, M. Saffman, and T. G. Walker, *Phys. Rev. Lett.* **112**, 043602 (2014).
- [15] V. M. Stojanović, *Phys. Rev. A* **103**, 022410 (2021).
- [16] T. Haase, G. Alber, and V. M. Stojanović, *Phys. Rev. A* **103**, 032427 (2021).
- [17] For a recent review, see L. Qi, J. Chiaverini, H. Espinós, M. Palmero, and J. G. Muga, [arXiv:2104.07362](https://arxiv.org/abs/2104.07362).
- [18] K. Nakagawa, Y. Suzuki, M. Horikoshi, and J. B. Kim, *Appl. Phys. B* **81**, 791 (2005).
- [19] T. P. Purdy, D. W. C. Brooks, T. Botter, N. Brahms, Z.-Y. Ma, and D. M. Stamper-Kurn, *Phys. Rev. Lett.* **105**, 133602 (2010).
- [20] S. Pandey, H. Mas, G. Drougakis, P. Thekkepatt, V. Bolpasi, G. Vasilakis, K. Poullos, and W. von Klitzing, *Nature (London)* **570**, 205 (2019).
- [21] S. Kuhr, W. Alt, D. Schrader, I. Dotsenko, Y. Miroshnychenko, W. Rosenfeld, M. Khudaverdyan, V. Gomer, A. Rauschenbeutel, and D. Meschede, *Phys. Rev. Lett.* **91**, 213002 (2003).
- [22] J. A. Sauer, K. M. Fortier, M. S. Chang, C. D. Hamley, and M. S. Chapman, *Phys. Rev. A* **69**, 051804(R) (2004).
- [23] D. Barredo, V. Lienhard, S. de Léséleuc, T. Lahaye, and A. Browaeys, *Nature (London)* **561**, 79 (2018).
- [24] M. O. Brown, T. Thiele, C. Kiehl, T.-W. Hsu, and C. A. Regal, *Phys. Rev. X* **9**, 011057 (2019).
- [25] For a recent review, see A. Browaeys and T. Lahaye, *Nat. Phys.* **16**, 132 (2020).
- [26] For an extensive review, see D. Guéry-Odelin, A. Ruschhaupt, A. Kiely, E. Torrontegui, S. Martínez-Garaot, and J. G. Muga, *Rev. Mod. Phys.* **91**, 045001 (2019).
- [27] H. R. Lewis and W. Riesenfeld, *J. Math. Phys. (N.Y.)* **10**, 1458 (1969).
- [28] See, e.g., J. Werschnik and E. K. U. Gross, *J. Phys. B: At. Mol. Opt. Phys.* **40**, R175 (2007).
- [29] C. Whitty, A. Kiely, and A. Ruschhaupt, *Phys. Rev. Research* **2**, 023360 (2020); [arXiv:2109.04420](https://arxiv.org/abs/2109.04420).
- [30] Q. Zhang, X. Chen, and D. Guéry-Odelin, *Phys. Rev. A* **92**, 043410 (2015).
- [31] D. Schrader, S. Kuhr, W. Alt, M. Müller, V. Gomer, and D. Meschede, *Appl. Phys. B* **73**, 819 (2001).
- [32] K. M. Fortier, S. Y. Kim, M. J. Gibbons, P. Ahmadi, and M. S. Chapman, *Phys. Rev. Lett.* **98**, 233601 (2007).
- [33] I. Dotsenko, W. Alt, M. Khudaverdyan, S. Kuhr, D. Meschede, Y. Miroshnychenko, D. Schrader, and A. Rauschenbeutel, *Phys. Rev. Lett.* **95**, 033002 (2005).
- [34] Y. Miroshnychenko, W. Alt, I. Dotsenko, L. Förster, M. Khudaverdyan, D. Meschede, D. Schrader, and A. Rauschenbeutel, *Nature (London)* **442**, 151 (2006).
- [35] M. Langbecker, R. Wirtz, F. Knoch, M. Noaman, T. Speck, and P. Windpassinger, *New J. Phys.* **20**, 083038 (2018).
- [36] D. A. Steck, *Rubidium 87 D-Line Data*, revision 2.2.2, 9 July 2021, [url: https://steck.us/alkalidata/rubidium87numbers.pdf](https://steck.us/alkalidata/rubidium87numbers.pdf).
- [37] See, e.g., M. D. Feit, J. A. Fleck Jr., and A. Steiger, *J. Comp. Phys.* **47**, 412 (1982).
- [38] See, e.g., A. D. Bandrauk and H. Shen, *J. Chem. Phys.* **99**, 1185 (1993).
- [39] See, e.g., R. Gilmore, *Lie Groups, Lie Algebras, and*

- Some of Their Applications*, (Dover Publications, 2012).
- [40] P. Pechukas and J. C. Light, *J. Chem. Phys.* **44**, 3897 (1966).
 - [41] W. H. Press, S. A. Teukolsky, W. T. Vetterling, and B. P. Flannery, *Numerical Recipes in C: The Art of Scientific Computing* (Cambridge University Press, Cambridge, 1999).
 - [42] See, e.g., K. Gottfried and T.-M. Yan, *Quantum Mechanics: Fundamentals*, 2nd ed. (Springer, New York, 2003).
 - [43] S. Martínez-Garaot, M. Palmero, D. Guéry-Odelin, and J. G. Muga, *Phys. Rev. A* **92**, 053406 (2015).
 - [44] M. Palmero, R. Bowler, J. P. Gaebler, D. Leibfried, and J. G. Muga, *Phys. Rev. A* **90**, 053408 (2014).
 - [45] V. M. Stojanović, C. Wu, W. V. Liu, and S. Das Sarma *Phys. Rev. Lett.* **101**, 125301 (2008).
 - [46] P. P. Hofer, C. Bruder, and V. M. Stojanović, *Phys. Rev. A* **86**, 033627 (2012).
 - [47] T. L. Chow, *Mathematical Methods for Physicists: A concise introduction* (Cambridge University Press, Cambridge, 2000).
 - [48] E. W. Weisstein, *Faà di Bruno's Formula*, in: MathWorld – A Wolfram Web Resource (Apr. 15, 2021). url: <https://mathworld.wolfram.com/FaadiBrunosFormula.html>.